Nivlisen, an Antarctic ice shelf in Dronning Maud Land: Geodetic-glaciological results from a combined analysis of ice thickness, ice surface height and ice flow observations

Martin Horwath[1], Reinhard Dietrich[1], Michael Baessler[1], Uwe Nixdorf[2], Daniel Steinhage[2], Diedrich Fritzsche[3], Volkmar Damm[4], Gernot Reitmayr[4]

[1] Technische Universität Dresden, Institut für Planetare Geodäsie, D-01062 Dresden, Germany, E-mail: horwath@ipg.geo.tu-dresden.de
[2] Alfred Wegener Institute for Polar and Marine Research, P.O. box 120161, D-27515 Bremerhaven, Germany
[3] Alfred Wegener Institute for Polar and Marine Research, P.O. box 600149, D-14473 Potsdam, Germany
[4] Federal Institute for Geosciences and Natural Resources (BGR), P.O. box 510153, D-30631 Hannover, Germany

Abstract

Extensive observations on Nivlisen, an ice shelf at Antarctica's Atlantic coast, are analysed and combined to achieve a new-quality description of its complex glaciological regime. We generate models of ice thickness (primarily from ground-penetrating radar), ellipsoidal ice surface height (primarily from ERS-1 satellite altimetry), freeboard height (by utilising precise sea surface information), and ice flow velocity (from ERS-1/2 SAR interferometry and GPS measurements). Accuracy assessments are included. Exploiting the hydrostatic equilibrium relation we infer the 'apparent air layer thickness' as a useful measure for a glacier's density deviation from a pure ice body. This parameter exhibits a distinct spatial variation (ranging from ≈ 2 m to ≈ 16 m) which we attribute to the transition from an ablation area to an accumulation area. We compute mass flux and mass balance parameters on a local and areally integrated scale. The combined effect of bottom mass balance and temporal change averaged over an essential part of Nivlisen is $-654 \pm 170 \ \mathrm{kg \, m^{-2} a^{-1}}$ which suggests bottom melting processes to dominate. We discuss our results in view of temporal ice mass changes (including remarks on historical observations), basal processes, near-surface processes, and ice-flow dynamical features. The question for temporal changes remains open from the data at hand, and we recommend further observations and analyses for its solution.

1   Introduction

1.1   Nivlisen

The ice shelves around Antarctica are important elements in the climate coupling of the Antarctic ice masses: The grounding line is the output gate for mass loss of the grounded ice sheet. The ice shelves themselves have intensive interactions with the atmosphere (through ice accumulation and ablation, radiation and albedo) and with the ocean (through bottom melting and freezing, iceberg calving). Hence, ice shelves are particularly sensible to climatic influences and changes.

Here we investigate Nivlisen which is one of the number of small ice shelves bordering Antarctica's Atlantic sector. Fig. 1 shows its geographic situation. The ice shelf extends over about 80 km in south-north and 130 km in west-east direction. Ice thicknesses vary from about 700 m in the southeast to 150 m at the ice front. At some locations the ice rests on the bedrock forming ice rises and ice rumples. The ice shelf is nourished by glaciers draining the inland ice of Wegenerisen through the mountains of Wohlthatmassivet. Typical flow velocities are in the order of $100 \ \mathrm{m\,a}^{-1}$.

The surface regimes and, accordingly, the upper layers' firn and ice structures vary significantly over Nivlisen. Its southeastern part belongs to a bare ice region extending over about 100 km in southeastern direction. It is predominantly a large ablation zone preserved by dry katabatic winds and summer melting due to the reduced albedo of bare ice. To the north, this region is followed by the transition to an extended accumulation zone. On the border between the inland ice and the ice shelf there is an ice-free area of bedrock (a so-called oasis) maintained due to the ablation regime of the surrounding ice. This area is called Schirmacheroasen.

The ice shelf can be considered in hydrostatic balance at positions a few kilometres away from grounded ice. This property is supported both by mechanical modelling (Rabus and Lang, 2002) and by observational evidence: SAR interferometry from the ERS-1/2 tandem mission shows distinct zones of vertical deformation along the grounding lines indicating that the ice shelf adapts to tidal and other sea level displacements along these zones and keeps its bulk in hydrostatic balance (Metzig and others, 2000; see also Sec. 2.3). Korth and others (2000) used several kinematic GPS tracks across the grounding zone to show in detail how the reaction to tidal displacements evolves from zero on the grounded side to the full tidal displacement in 2 to 4 km distance.

Not least due to the logistic basis provided by the Soviet/Russian, Indian, and former

German (GDR) research stations in Schirmacheroasen the region has been the subject of extensive geoscientific investigations for decades. Bormann and Fritzsche (1995) give a comprehensive review of the works until the beginning of the 1990-s. Since that time, especially geodetic-glaciological field observations have been widely extended. New types of satellite-aided observations have become available, such as Global Positioning System (GPS) measurements on ground and satellite altimetry and synthetic aperture radar (SAR) interferometry from space.

This paper analyses a part of these newer observations which now allow a more extensive, more detailed and more accurate description of Nivlisen's glaciological regime than presented so far. After a description of our basic observations and their processing (Sec. 2) we present in Sec. 3 the additional inferences from combining the individual types of data under two aspects: hydrostatic equilibrium and mass balance. (These fundamental links between major ice shelf parameters are briefly reviewed in Secs. 1.2 and 1.3.) In Sec. 4 we discuss our findings addressing the spatially varying firn conditions visible from the hydrostatic balance relation, basal processes and possible temporal changes, the interplay between snow accumulation and compaction and dynamical ice flow conditions.

1.2 Hydrostatic balance of ice shelves

Free floating of an ice shelf implies the hydrostatic balance relation

$$\rho_w(Z - h) = \overline{\rho}Z, \tag{1}$$

where Z is the total ice thickness, h the surface height above see level (freeboard height), ρ_w the mean density of the displaced sea water column, and $\overline{\rho}$ the mean density of the ice shelf column.

This relation has been widely exploited in ice shelf studies. See, e.g., Renner (1969) for an early review and Coslett and others (1975) or Shabtaie and Bentley (1982) for the methodology adopted here. Through hydrostatic balance, surface heights were derived from ice thicknesses (Bamber and Bentley, 1994) and ice thicknesses from surface heights (Vaughan and others, 1995) or geopotential models were locally evaluated by the hydrostatic balance requirement (Shabtaie and Bentley, 1987; Jenkins and Doake, 1991). Apparent violations of hydrostatic balance gave indications for grounding (Shabtaie and Bentley, 1987), for varying firn and ice structures (Budd and others, 1982; Bamber and Bentley, 1994), for sediments transported by the ice (Thyssen and Grosfeld, 1988), or for marine ice frozen to the shelf ice bottom (Thyssen, 1988; Jenkins and Doake, 1991).

Eq. 1 may be reformulated in the form

$$\rho_w(Z - h) = \rho_i(Z - \delta), \tag{2}$$

where ρ_i is the density of pure ice and δ is defined by

$$\delta = \int_0^Z \frac{\rho_i - \rho(z)}{\rho_i} dz = \frac{\rho_i - \overline{\rho}}{\rho_i} Z. \tag{3}$$

That is, δ is the relative deviation of the ice shelf density ρ from the pure ice density ρ_i, integrated along the ice column. Resolved for its three main constituents, Eq. 2 reads

$$\delta = \frac{\rho_w}{\rho_i} h - \frac{\rho_w - \rho_i}{\rho_i} Z, \tag{4}$$

$$h = \frac{\rho_w - \rho_i}{\rho_w} Z + \frac{\rho_i}{\rho_w} \delta, \tag{5}$$

$$Z = \frac{\rho_w}{\rho_w - \rho_i} h - \frac{\rho_i}{\rho_w - \rho_i} \delta. \tag{6}$$

In the common case that an ice shelf consists in a mixture of pure fresh water ice and air, the meaning of δ is plausible: A (fictive) rearrangement of the ice shelf into a body of solid ice and a layer of air would result in the solid ice thickness

$$Z_i = Z - \delta \tag{7}$$

and the air layer thickness δ. Since most of the air is contained in the upper firn layers δ depends on the accumulation and densification regime but does not (or little) depend on the total ice thickness. The mean density $\overline{\rho}$, in contrast, depends on both. Values of air layer thicknesses δ reported in the literature cited in this section vary between 10 m and 20 m.

If the ice shelf consists not only of fresh water ice and air then δ does not mean the air layer thickness. Therefore, δ is called the 'apparent air layer thickness' in the following. If, e.g., a marine ice layer of thickness Z_{mar} and density $\rho_{\mathrm{mar}} > \rho_i$ is frozen to the bottom of a meteoric ice part of thickness Z_{met} then Eq. 3 reads

$$\delta = \int_0^{Z_{\mathrm{met}}} \frac{\rho_i - \rho(z)}{\rho_i} dz + \int_0^{Z_{\mathrm{mar}}} \frac{\rho_i - \rho_{\mathrm{mar}}}{\rho_i} dz = \delta_{\mathrm{air}} + \delta_{\mathrm{mar}}. \tag{8}$$

δ is now the sum of the air layer thickness δ_{air} and a negative correction δ_{mar}. However, since $\rho_{\mathrm{mar}} \approx 925$ kg m^{-3} exceeds ρ_i only slightly (see Sec. 2.4), $\delta_{\mathrm{mar}} \approx -0.02 \, Z_{\mathrm{mar}}$ tends to be small. Sediments enclosed in the lower ice shelf layers are another possible phenomenon that adds a negative contribution to δ and may even cause δ to be negative in total.

The apparent air layer thickness δ when computed from surface height and ice thickness through Eq. 4 is a useful indication on density structures and on the validity of the

free float assumption. At the same time it is very sensitive to errors in the input data, in particular Z and h. Gross errors in Z may arise if a marine ice layer is not recorded in the measurement as may happen with radar techniques. Biases in the freeboard height h may arise from uncertainties in the geoid and sea surface topography data needed to reduce ellipsoidal heights to freeboard heights. Therefore, δ has been frequently treated as the combination of the air layer thickness and an unknown height bias.

Once δ is known for a certain region of free floating, the relation between ice thickness and freeboard height is established and can be exploited accordingly.

1.3   Mass flux and mass balance on ice shelves

The mass conservation equation for a vertical column of an ice shelf (Paterson, 1994) can be written as

$$
\begin{aligned}
b_s + b_b - \rho_i \frac{\partial Z_i}{\partial t} &= \operatorname{div}(\rho_i Z_i \boldsymbol{u}) \\
&= \rho_i \left[Z_i \left(\frac{\partial u}{\partial x} + \frac{\partial v}{\partial y} \right) + u \frac{\partial Z_i}{\partial x} + v \frac{\partial Z_i}{\partial y} \right].
\end{aligned}
\tag{9}
$$

Here, b_s and b_b (in units of mass per surface area per time, positive for mass gain) are the surface mass balance and the basal mass balance, respectively, Z_i is the solid ice thickness (Eq. 7), $\rho_i \partial Z_i / \partial t$ is the local ice mass change with time, and $\boldsymbol{u}$ is the depth-independent horizontal flow velocity vector with components u and v in the x and y coordinate directions, respectively. According to Bamber and Payne (2003), we call $b_s + b_b$ the specific mass balance and $\rho_i \partial Z_i / \partial t$ the local mass balance. Their integral effect over a certain region A can be computed through Gauß' theorem by balancing the ice in-flux and out-flux across the region boundaries:

$$
\iint_A \left(b_s + b_b - \rho_i \frac{\partial Z_i}{\partial t} \right) d\sigma = \int_K |\rho_i Z_i \boldsymbol{u}| \sin \beta \, ds,
\tag{10}
$$

where K is the boundary curve oriented anti-clockwise, and β is the (anti-clockwise) angle between K and the velocity $\boldsymbol{u}$. Conveniently, some sections of K follow flowlines where the integral vanishes and other sections form the fluxgates.

The basal balance b_b is commonly the most uncertain mass balance term. The above equations may constrain it based on the geometric magnitudes of ice thickness, freeboard height and ice flow velocity.

5

2 Data

2.1 Ice thickness

Fig. 2 gives an overview of ice thickness observations on Nivlisen. In this study we used data from the three sources shown by tracks in Fig. 2: A radar system operating from a helicopter was used by the German Federal Institute for Geosciences and Natural Resources (BGR) during the GEOMAUD expedition in 1995/1996 (Damm and Eisenburger, 2005). A similar instrumentation but mounted on an airplane was used by the Alfred Wegener Institute for Polar and Marine Research Bremerhaven (AWI) in the same summer season (Meyer and others, 2005; Steinhage and others, 1999). Finally, radar measurements along a ground traverse crossing the east of the ice shelf were carried out by the AWI in 1992 (Fritzsche, 2005).

The relative precision of the ice thickness measurements was estimated to be 1% to 2%. In a crossover analysis for all radar tracks (including grounded ice) crossover differences at 61 positions, divided by the absolute thicknesses, showed an rms value of 4.5%. This number is affected by errors of the measurement positions and of the interpolation to crossover points which both, in turn, depend on along-track variations of the measurements. The ice thickness tracks on Nivlisen seem to have two regimes of fluctuation, with a distinct border along approximately $-70.35°$ latitude (see Fig. 8 for an example): In the south, fluctuations are high with typically 10 to 20 m differences between 300 m distant track points. In the north, the thickness curves are smooth, in contrast. Accordingly, the rms of 9 relative crossover differences in the northern part is 1.9% indicating a measurement precision of $1.9\%/\sqrt{2}$ =1.4%, i.e., typically 1.4% $\times$ 350 m = 4.9 m. In what follows we will rely on thickness data with a reduced resolution of 3.7 km. For these data a relative precision of 1.4% seems realistic over the entire ice shelf.

Despite this precision, biases in the thickness data have to be considered. The along-track fluctuations in the southern part may indicate a complex (e.g., crevassed) structure of the ice shelf bottom with associated ambiguities in the radar echo. We estimate the inaccuracy resulting from these effects to be up to 4.4% of ice thickness. Variance combination with the above 1.4% precision leads to a total uncertainty of $\sqrt{4.4^2 + 1.4^2}\,\% = 4.6\,\%$ in the southern part, i.e., typically 4.6% $\times$ 450 m = 21 m. Another bias in the initial ice thickness data results from using the signal propagation velocity for ice ($168\cdot10^6\ \mathrm{m\,s^{-1}}$) in the radar processing. In Sec. 3.2 we will apply the correction for the higher velocities

in firn.

Ice thickness data from other measurements (see Fig. 2) were analysed but not included in the further computations: During the 1995/1996 GEOMAUD expedition ice thickness was measured at 10 ground positions on Nivlisen by radar sounding and partly also by seismic sounding (Reitmayr, 1996). For part of the data the interpretation of the signal return from only a single point measurement is ambiguous. In 1975/1976 groups of Soviet Antarctic Expeditions performed two ice core drillings through the ice shelf and a third one through the nearby grounded ice (Korotkevich and others, 1978). In the same years, radio echo soundings were carried out both from airplanes (Kozlovskii and Fedorov, 1983) and along ground traces (Boyarskii and others, 1983; Eskin and Boyarskii, 1985). Differences between these historical data and the models derived hereafter will be further addressed in Sec. 4.3.

2.2 Ice surface height

2.2.1 Ellipsoidal height

Ellipsoidal heights were observed by satellite altimetry and by GPS measurements. Fig. 3 gives an overview.

We performed a dedicated analysis of ERS-1 data of the geodetic mission phase E/F (April 1994 to March 1995) processed by the French Centre Nationale d'Etudes Spatiales (CNES) (Rémy and others, 1999). The data contain geophysically corrected and retracked ellipsoidal heights at satellite subtrack positions together with the waveform parameters of the leading edge, the trailing edge and the backscatter obtained in the retracking procedure.

At the steep transition between floating ice and grounded ice the altimeter tracker fails to follow the surface. This leads to an interruption of tracks along the grounding zone. In contrast to continental-scale processings, no attempt was made to interpolate heights across this gap, but only measurements on the ice shelf were used. Moreover, to avoid slope errors due to the poorly known slopes of the adjacent grounded ice, positions near the grounding line were excluded. The minimum distance was set to 8 km, allowing for 0.02 radians slope beyond the grounding line.

Strongly reflecting targets such as meltwater surfaces can divert the on-board tracker from tracking the nearest surface points. Such instances are indicated by exceptionally high backscattering coefficients σ^0 and steep trailing edge slopes Fl of the altimeter

waveform. Hence, measurements exceeding $\sigma^0 = 30$ dB or $Fl = -0.024$ dB per gate (1 gate = 3 ns) were rejected and their neighbouring positions were checked for obvious corruptions.

Static GPS measurements were carried out during the GEOMAUD expedition in 1995/1996 (Reitmayr, 1996). Their vertical precision is better than 10 cm. Kinematic GPS measurements along a ground traverse through the eastern part of Nivlisen were carried out in 1998 by Technische Universität Dresden (Korth and others, 2000). The accuracy of the processed heights is better than 5 cm.

2.2.2 Reductions to freeboard height: geoid, sea surface topography, and tides

The transformation from ellipsoidal heights H to the freeboard heights h needed in the hydrostatic balance relation reads

$$h = H - (N + \zeta_{\text{SST}} + \zeta_{\text{Tides}}) \tag{11}$$

where the geoid height N represents the height of a (hypothetic) ocean at rest, the sea surface topography (SST) ζ_{SST} describes the deviation from the geoid due to ocean dynamics and density variations, and ζ_{Tides} denotes the tidal displacement of the sea surface and, correspondingly, of the freely floating ice.

The geoid height N is the largest correction term. Thanks to the new satellite gravity missions CHAMP (launched in 2000), GRACE (launched in 2002), and GOCE (to be launched in 2006) the accuracy of global geoid models is drastically improving, in particular over Antarctica. Further refinements may be achieved with airborne and ground observations. For Nivlisen, such a refinement is available by a regional geoid model (Korth and others, 1998) derived from surface gravimetry together with airborne and ground-based ice thickness measurements. Its estimated accuracy is 50 cm for the absolute geoid level and 7 cm for the geoid variations within the model domain. Fig. 4 shows a regional comparison between the geoids according to EGM96 (a state-of-the-art geopotential model before the new missions), preliminary CHAMP and GRACE models, and the regional model. All models show an average level of 15 to 18 m over the region, with EGM96 deviating most from the regional model. The larger-scale variations of the regional model are comparably well reproduced by the GRACE model and by EGM96 although the preliminary GRACE model uses only 39 days of satellite observations while EGM96 includes virtually all information available by 1996. However, even with its full

performance GRACE will not resolve small-scale geoid variations, due to their attenuation at satellite height. In the following, we use the regional geoid model as the best available source. By adding the permanent tide effect of -0.19 m it is transformed from the tide-free to the mean-tide system to be consistent to the ellipsoidal height data.

For ζ_{SST}, we use the large-scale model estimated simultaneously with the EGM96 geopotential model from the combination of satellite altimetry, satellite tracking data and gravimetric data (Lemoine and others, 1996) which gives a value of -1.7 m for Nivlisen. The geoid to which the EGM96 SST refers has a different reference gravity potential ($W_0 = 6.263685857 \cdot 10^7 \ \mathrm{m^2 s^{-2}}$) than our regional geoid model ($W_0 = 6.263686085 \cdot 10^7$ $\mathrm{m^2 s^{-2}}$, according to GRS80). Hence, the SST height was corrected by the respective height difference (23 cm) to a value of -1.47 m (see, e.g., Smith, 1998, for the subtleties of geoid heights). Smaller scale features of the SST are not corrected and enter the error budget: The uncertainties that we assign to the SST model are 0.3 m for its absolute level and 0.14 m for its spatial variations.

Temporal variations of the SST are not corrected. Their largest part is the ocean's inverse barometric effect. This effect was verified from tide gauge observations and had an rms in the order of 13 cm (Dietrich and others, 1995; Dietrich and others, 1998). We estimate the total rms of temporal variations to be 0.2 m.

The tidal displacements ζ_{Tides} of the freely floating ice shelf are predicted from a precise tidal model. It was derived from 15 months of tide gauge observations in an epishelf lake in Schirmacheroasen which is linked to the ocean (Dietrich and others, 1995; Dietrich and others, 1998). The applicability of this model to the entire Nivlisen was validated by kinematic GPS observations at several positions on the ice shelf (Korth and others, 2000). After reduction of the inverse barometric effect, the residual rms error of predicted tides was 4 cm.

2.2.3 Compiled elevation models

From the altimetry data that passed the selection described in Sec. 2.2.1 (see Fig. 3) a model of the temporal mean ellipsoidal heights on Nivlisen was generated with a continuous curvature spline algorithm (Wessel and Smith, 1991). Heights on floating ice were corrected in advance for their instantaneous tidal displacements. The slope error was corrected by the simple slope correction method (Brenner and others, 1983). Since the computation of surface slopes already requires a topography model, the model generation was iterated. The resulting topography model has a resolution of $6' \times 2'$, i.e., about $3.7 \times$

3.7 km². It thus reflects heights averaged in a 3.7 km scale. Values at arbitrary positions within the model domain are obtained by bicubic interpolation.

A rough error estimation of the model is summarised in Tab. 1. We distinguish several kinds of errors: First, errors in the altimetric data arise from orbit errors, errors in the tropospheric delay correction, instrument noise and, most importantly, the complex effects of surface roughness and penetration on the retracked heights (Rémy and others, 1999). The rms of these errors is estimated to be 0.4 m. Second, uncorrected temporal SST variations may not fully average out. They were assigned with an rms of 0.2 m in Sec. 2.2.2. Third, the limited spatial resolution and coverage of the measurements affects the model accuracy. The resolution results not only from the sampling but as well from the 3 km scale pulse-limited footprint of the ERS altimeter. The applied slope correction does not consider surface curvature effects but an additional curvature correction (Brisset and Rémy, 1996) would exceed 10 cm only in the area north of the ice rumple about 10.7°E, −70.4°S where the topography is probably too complex for this correction to apply. Near the boundary of the model domain, interpolation of heights turns into extrapolation providing an additional error source. Based on the available information on smaller-scale slopes and curvatures (Wiehl and Dietrich, 2000) we estimate the rms error due to the limited spatial sampling to be 0.8 m for point heights and 0.5 m for the 3.7 km scale averages represented by the model, except for positions near the domain boundary and the above-mentioned ice-rumple where our estimate is 1.5 m. Combining the three estimated errors in the sense of variance combination, we estimate the rms error of the model to be 0.67 m (0.92 m for point heights) in general and 1.6 m near the domain boundary and the ice-rumple.

For an internal validation, a crossover analysis of the selected data revealed an rms crossover difference of 0.51 m, supporting the error estimate for the altimetric data plus uncorrected temporal variations. For an external validation, the altimetric model was compared to the GPS heights. The rms difference to the 9 static GPS measurements in the altimetric model domain was 0.82 m supporting the estimated 0.92 m error for point heights. A comparison to the kinematic GPS measurements along the traverse is shown in Fig. 5. It shows agreement within one metre except for the two margins. In the northwestern part near the ice front the altimetric model smoothes the topographic details of the ice rumples. In the southern part extrapolation near the altimetric domain boundary causes larger errors.

The GPS heights (after their tidal correction at floating ice positions) were then added

to the altimetric data to yield ellipsoidal height model with extended data support and coverage.

Finally, the modelled ellipsoidal heights at floating positions were reduced by the geoid height and the constant part of the SST to obtain freeboard heights. The errors of this freeboard height model (Tab. 1) arise from variance combination of the ellipsoidal height model errors and the errors in the freeboard height corrections discussed in Sec. 2.2.2.

2.3 Ice flow velocity and grounding zone

2.3.1 Observations

Interferometric processing of satellite synthetic aperture radar (SAR) data was applied to infer a two-dimensional high resolution data set of horizontal flow velocities as well as the limits of the grounding zones. Two ascending, partly overlapping ERS-1/2 stripes were acquired over Nivlisen during the tandem mission in May 1996 (Tab. 2). The temporal baseline of exactly one day between subsequent acquisitions as well as a relatively short interferometric baseline yield good coherence in both interferograms. In addition to the SAR data, ice flow velocities were observed by repeated GPS observations in 1992 and 1993 in the northeast of the ice shelf (arrows in Fig. 7). The velocities and flow directions have an accuracy of $2 \, \mathrm{m \, a^{-1}}$ and $2.5°$, respectively (Korth and Dietrich, 1996), which is very suitable for calibration purposes.

2.3.2 SAR processing

The SAR sensors of the ERS-1/2 satellites peer perpendicular to the flight direction with an approximate incidence angle of $23°$. Due to the sensor's principle of operation only changes in its line of sight can be observed. Consequently, the inference of the three-dimensional flow vector or even of its two horizontal components needs additional information. Utilising the different views of ascending and descending passes is a typical approach to overcome this problem. However, even if interferograms from descending passes were available, this method would be very difficult to apply over floating ice because different vertical displacements between acquisitions cause significant phase changes. Although a precise tide model exists for Nivlisen (see Sec. 2.2.2), air pressure differences and, hence, the inverse barometer reaction are unknown. However, if flow directions are known they can be deployed in conjunction with the assumption of

surface-parallel flow to add the needed information. Of course, this technique is also sensitive to ocean-induced vertical changes. But under the assumption that those vertical changes are uniform over the ice shelf their effect cancels out when tying the velocity field to an absolute reference. Phase gradients of the interferogram can be used to verify this assumption and, moreover, can be exploited to discover regions of stronger non-uniform deformation.

For most parts of Nivlisen, flowlines could be identified in the low-pass filtered geocoded SAR amplitude image (see Fig. 6a). They were digitised and their directional information was interpolated to a grid of flow azimuths. By combination with surface slopes calculated from the DEM derived in this study (Sec. 2.2.3 and 3.2), three-dimensional flow directions were obtained.

The interferograms were calculated and their phase gradients were determined (Fig. 6b). They support the assumption of a nearly uniform vertical displacement of the floating ice. Moreover, grounding zones can be clearly detected by the larger gradients induced by inhomogeneous vertical deformations. Upper and lower limits of flexure were mapped and used to mask out areas of non-uniform vertical deformation.

The effects of earth curvature and topography were corrected by subtracting a synthetic interferogram calculated using precise ERS orbits (Scharroo and others, 1998) and our DEM. The remaining interferogram (Fig. 6c) should include deformation effects only. After masking out grounded areas, grounding zones and regions with disrupted phase values, the modulo 2π phase was unwrapped by the branch cut method (Goldstein and others, 1988) to obtain absolute phase differences which represent the projection of flow velocity differences onto the SAR line of sight. Then, using the three-dimensional flow direction, all three components of the displacement vectors were calculated. Each interferogram was processed separately in this way. In the region of overlap the final product was generated by an average with linearly changing weights. Then the relative velocity field obtained so far was referenced to absolute values by the GPS ground truth observations.

2.3.3 Results

Fig. 7 presents the obtained horizontal velocity field for Nivlisen.

In order to assess the accuracy of the applied technique, we consider that the horizontal velocity $|\boldsymbol{u}|$ is basically a function of three observations: the range change in the satellite's line of sight (divided by the temporal baseline), r, the angle between the flow

direction and the satellite's line of sight azimuth, α, which is inferred from the digitised flow directions, and the surface slope β inferred from the DEM employed. Neglecting the comparatively small effect of β, the functional relation is

$$|\boldsymbol{u}| = r \sin^{-1} \theta \cos^{-1} \alpha \qquad (12)$$

where the radar incidence angle θ is precisely known. Those regions where $74° < \alpha < 106°$, i.e., where the factor $\cos^{-1} \alpha$ leads to more than 350% error magnification were masked out a priori. An error propagation from r and α to $|\boldsymbol{u}|$ was then computed by

$$\sigma^2_{|\boldsymbol{u}|} = (\partial |\boldsymbol{u}| / \partial r)^2 \sigma^2_r + (\partial |\boldsymbol{u}| / \partial \alpha)^2 \sigma^2_\alpha. \qquad (13)$$

The error σ_α of the digitised flow lines was estimated to be $5°$. An evaluation of σ_r is more difficult since any errors of the interferometric analysis (such as co-registration and interpolation errors, DEM and baseline errors or atmospheric or ionospheric influences) propagate into r. Under reference to the precise orbits of Scharroo and others (1998) and to the stochastic model for radar interferometry by Hanssen (2001) an estimated range change error of $1/4$ of a fringe, leading to $\sigma_r = 2.6 \text{ m a}^{-1}$, seems reasonable. Fig. 6d depicts the resulting velocity error $\sigma_{|\boldsymbol{u}|}$. Its variations are predominantly induced by variations in α.

These error estimates were supported by a comparison between the two SAR tracks in their region of overlap which indicated an even slightly better precision. However, one should bear in mind that the only absolute reference for the entire velocity field are the three GPS points in the northeast, matching with $\pm 3.1 \text{ m a}^{-1}$. Since the assumption of a uniform vertical displacement of the ice shelf is certainly only an approximation, residual deformations wrongly interpreted as ice flow may cause additional errors.

The detected grounding zone limits (see Sec. 2.3.2 and Fig. 6) are used as criteria for free float later in this study: Seaward from the flexure zones the ice is considered to be in hydrostatic balance. Low tide limits are used where they differ from high tide limits. In our maps, however, we depict the most landward flexure limits to indicate the grounding line.

2.4 Surface mass balance and density data

As mentioned in Sec. 1.1, Nivlisen is divided into an ablation zone in the southeast and an accumulation zone in its remaining parts. Accumulation is due to both precipitation and drift snow. Part of the accumulated snow melts in summer and percolates into deeper horizons forming ice layers and lenses there (Bormann and Fritzsche, 1995).

Ablation rates were observed over up to 5 years (1988-1993) at stakes along two traverses through the grounded part of the ablation area (Korth and Dietrich, 1996). The mean ablation at 47 stakes was 230 $\mathrm{kg\,m^{-2}a^{-1}}$ with a 100 $\mathrm{kg\,m^{-2}a^{-1}}$ standard deviation of the spatial variations. For the close vicinity of Schirmacheroasen, Simonov (1971) reported 340 $\mathrm{kg\,m^{-2}a^{-1}}$ ablation. Accumulation rates along the traverse crossing the ice shelf (cf. Fig. 2) were measured between 1992 and 1993 at 7 stakes. The mean value is 316 $\mathrm{kg\,m^{-2}a^{-1}}$. Simonov (1971) reported a mean accumulation rate of 230 to 240 $\mathrm{kg\,m^{-2}a^{-1}}$ in the years 1959 to 1965. Summing up these references the surface mass balance is typically (-250 ± 100) $\mathrm{kg\,m^{-2}a^{-1}}$ in the ablation zone and $(+300 \pm 100)$ $\mathrm{kg\,m^{-2}a^{-1}}$ in the accumulation zone.

Density information is available down to 610 m depth from a deep core drilling in the grounded accumulation area south of Schirmacheroasen (Kislov and others, 1983). This data together with densities from a nearby shallow ice core (Fritzsche, 1996) may be fitted by the exponential relation (Paterson, 1994)

$$\rho(z) = \rho_i - (\rho_i - \rho_s)\exp(-Cz) \tag{14}$$

with the depth z, the surface snow density $\rho_s = 420\ \mathrm{kg\,m^{-3}}$ and the densification parameter $C = 0.029\ \mathrm{m^{-1}}$. The resulting air layer thickness from this fit is $\delta \approx (\rho_i - \rho_s)/(\rho_i C) = 18.7\ \mathrm{m}$ On the ice shelf itself, densities down to 15 m depth were observed from three ice cores (see Fig. 2 for locations) by the 1982/1983 Soviet Antarctic Expedition (Khokhlov, 1984). South, in the ablation area, vertically homogeneous ice with a large amount of air bubbles and a mean density of 879 $\mathrm{kg\,m^{-3}}$ was found. In the transition zone from the ablation to the accumulation regime, the ice below 12 metres resembled the ice in the ablation zone while the upper 12 metres consisted of both ice and consolidated firn. The third core near the ice front contained frozen firn of 640 $\mathrm{kg\,m^{-3}}$ density in 10 to 15 metres depth. In the upper ten metres ice layers dominated in the interchange with firn layers. These cores may illustrate the complexity and spatial variability of meteorological influences on the firn and ice structure.

For the densities of ocean water, ρ_w, and pure fresh water ice, ρ_i, needed for hydro-static balance considerations we use the values $\rho_w = 1029\ \mathrm{kg\,m^{-3}}$ and $\rho_i = 917\ \mathrm{kg\,m^{-3}}$. Ocean water densities applied, e.g., by Jenkins and Doake (1991), Shabtaie and Bentley (1982), and Vaughan and others (1995) at different ice shelves differ slightly between 1027.5 and 1030 $\mathrm{kg\,m^{-3}}$ indicating an uncertainty of 1.5 $\mathrm{kg\,m^{-3}}$ in our value. The pure ice density ρ_i applied in the works cited above differs between 915 and 920 $\mathrm{kg\,m^{-3}}$. We

assign an uncertainty of 3 kg m^{-3} to our pure ice density value. In hypothetic computations assuming a marine ice layer (Sec. 1.2 and 4.3) we use the marine ice density $\rho_{\mathrm{mar}} = 925$ kg m^{-3} according to Jenkins and Doake (1991).

3 Derived glaciological information

For the combined analysis of the various kinds of data compiled in Sec. 2 we assume that all included observations represent the state at one and the same epoch (say, 1/1/1996). Although they are actually obtained in a certain time span—mainly from 1992 to 1998—temporal variations of the observables are considered to be small compared to the errors of the observations themselves. The issue of temporal changes will be further discussed in Sec. 4.2.

3.1 Spatial variations of the hydrostatic balance parameter δ

To exploit the hydrostatic balance relation between ice thickness and freeboard height we selected those thickness measurements lying in the domain of our freeboard height model and on the freely floating ice shelf according to the limits explained in Sec. 2.3.3. For these positions we applied Eq. 4 to compute the apparent air layer thickness δ. Fig. 8 illustrates the result for the data along one radar track. From the irregularly distributed values of δ a gridded model was derived by a continuous curvature spline algorithm (Wessel and Smith, 1991). This model, shown in Fig. 9, is aimed to represent δ in the sense of 3.7 km scale averages.

Clearly, δ shows a large spatial variation with a distinct pattern: In the southeast of the ice shelf the values vary in general between 1 and 4 m. To the northwest of this region, δ increases from 4 to 14 m within a distance of about 22 km. Northwest of this zone of increase the values are in general between 14 and 20 m.

Tab. 3 summarises an error assessment for δ obtained by variance propagation from the errors of the individual inputs of Eq. 4. We consider the total error as a sum of the error of the spatial variations and the error of the absolute level. In particular, errors in ρ_w and ρ_i induce errors in δ which are proportional to $Z - h$, i.e., positive everywhere. Therefore, the error propagated from ρ_w and ρ_i is the sum of a constant part associated with the mean value of $Z - h$ and a spatially varying part associated with the spatial variations of $Z - h$. Errors of interpolating and slightly extrapolating δ (last line but one) are roughly estimated from the local variability of δ. In result, the estimated errors

in the spatial variations of δ are 2.8 m or less. The discovered variation of δ is, hence, much larger than its uncertainty and must reflect a geophysical signal.

3.2   Improved ice thickness and height information

In Sec. 4.1 we will argue that the obtained model for δ can in fact be considered to represent the air layer thickness. In anticipation of this outcome we use the information on firn density inherent in δ to determine the firn correction ΔZ for the ice thickness measurements (see Sec. 2.1). It can be given as

$$\Delta Z = \frac{n_i - 1}{n_i}\delta, \tag{15}$$

(Jenkins and Doake, 1991) with the pure ice refractive index $n_i = 1.78$. Strictly speaking, also the values for δ computed with the uncorrected ice thicknesses have to be corrected: With δ_m denoting the values computed with the uncorrected ice thicknesses we have

$$\delta = \delta_m + \Delta\delta, \tag{16}$$

where the correction $\Delta\delta$ is given through Eq. 4 by

$$\Delta\delta = -\frac{\rho_w - \rho_i}{\rho_i}\Delta Z. \tag{17}$$

From the last three equations we find

$$\Delta Z = \left(\frac{n_i}{n_i - 1} + \frac{\rho_w - \rho_i}{\rho_i}\right)^{-1} \delta_m = 0.416\ \delta_m \tag{18}$$

$$\Delta\delta = -\left(\frac{n_i}{n_i - 1}\frac{\rho_i}{\rho_w - \rho_i} + 1\right)^{-1} \delta_m = -0.051\,\delta_m. \tag{19}$$

That is, in the northwestern part of Nivlisen ΔZ is about 7 m. Corrected values for Z and δ are used in the further analyses as well as in the above Figs. 8 and 9.

Now, by the parameter δ, we know the spatially varying relationship between ice thickness and ice surface height and can use this knowledge to transform heights into ice thicknesses and vice-versa, thus improving our information on both.

Thus, an ice thickness model (Fig. 10) was generated merging direct observations and height data at floating positions converted to ice thicknesses (Eq. 6) using the established model of δ. The model domain was extended to the grounded ice east of Nivlisen where a satisfyingly dense coverage with original thickness measurements is available. The resolution is, again, about 3.7 km.

For an error estimation of the obtained ice thicknesses, a simple error propagation from all inputs of Eq. 6 would mean an overestimation because, by the genesis of the δ

model, systematic errors of δ are correlated with errors in ρ_w, ρ_i and the absolute level of the freeboard correction $(N + \zeta_{\mathrm{SST}} + \zeta_{\mathrm{Tides}})$ in a way that they cancel out largely in Eq. 6. Therefore, only the errors of the spatial variations of h and δ (see Tab. 1 and 3) were propagated. In result, the estimated error of ice thicknesses derived from heights is 23 m in general and 27 m near the model margin and the ice rumple about 10.7°E, -70.4°S. The latter value is also reasonable for the eastern ice shelf margin where thicknesses were interpolated over larger distances. For a model of the solid ice thickness $Z_i = Z - \delta$ the accuracy is practically the same as for Z.

Analogously, an ellipsoidal height model (Fig. 11) was generated from both direct height measurements and ice thickness data converted to heights through Eq. 5. In this way the model described in Sec. 2.2.3 could be extended in particular at the eastern ice shelf margin. At grid cells without original thickness observations we used the ice thickness model.

Concerning the errors of heights converted from thicknesses, an analogous argumentation applies as for thicknesses obtained from heights. Propagating only the errors of Z and the errors in the spatial variations of δ, we estimate the error of the obtained heights to be 3.8 m.

3.3   Mass flux and mass balance

Fig. 12 shows the horizontal ice mass flux on Nivlisen computed from the models of solid ice thickness and of horizontal flow velocity. Visual inspection suggests that the ice body loses mass while flowing northwards.

For a quantitative assessment of this loss, the net effect of specific mass balance and local mass balance, $b_s + b_b - \rho_i \partial Z_i / \partial t$, was evaluated through Eq. 9. Fig. 13a shows the result. At the same time, its spatially varying accuracy is indicated by dashed brown contours.

For this accuracy estimation we expressed the velocity components u and v of Eq. 9 through the two original observables r (velocity in the radar line of sight) and α (flow direction; see Sec. 2.3.3). Then we performed an error propagation from the errors of r, α and Z_i (23 m, 2.6 m a^{-1} and 5°, respectively, according to Secs. 3.2 and 2.3.3) and from the errors of their spatial derivatives. Those errors were roughly estimated to be 2 m km^{-1} for $\partial Z_i / \partial x$, $\partial Z_i / \partial y$, 0.2 m a^{-1}km^{-1} for $\partial r / \partial x$, $\partial r / \partial y$, and 0.7°km^{-1} for $\partial \alpha / \partial x$, $\partial \alpha / \partial y$. The largest contributions to the error of $b_s + b_b - \rho_i \partial Z_i / \partial t$ originate from the spatial derivatives of flow direction and of velocity.

The mass balance magnitudes in Fig. 13a are negative at most places. However, they show a very variable pattern and have large uncertainties. To obtain more significant information we performed a massflux evaluation (Eq. 10) over the three areas A, B, and C shown in Fig. 13b. Tab. 4 lists the results. Accounting for the known surface mass balance (Sec. 2.4) we find that, in an average over the three areas, the combined effect of basal mass balance and temporal change is $-654 \pm 170 \ \mathrm{kg\,m^{-2}a^{-1}}$.

A rigorous error propagation for the integration in Eq. 10 would need spatial correlation information on the error of the integrand $|\rho_i Z_i \boldsymbol{u}| \sin\beta$. Our error assessment for each area assumes uncorrelated errors of the fluxes through its four boundary sections: upstream, downstream, and the two lateral flowline boundaries where zero cross-flux is expected but subject flow direction errors ('lateral in- and out-flux' in Tab. 4). Along each section, we compute the cross-flux error as the integral of the one-sigma error $\sigma_{|\rho_i Z_i \boldsymbol{u}| \sin\beta}$, thus allowing for full error correlation within the section. ($\sigma_{|\rho_i Z_i \boldsymbol{u}| \sin\beta}$ equals $|\rho_i Z_i \boldsymbol{u}| \sigma_\beta$ for flowline sections and $\sigma_{|\rho_i Z_i \boldsymbol{u}|}$ for the perpendicular fluxgates.) Area C covers part of the flow across the grounding line. Surface velocities of the grounded ice are known with $5 \ \mathrm{m\,a^{-1}}$ accuracy from the interferometric analysis of SAR observations from the ERS-1/2 tandem mission (Baessler and others, 2003). Here, the depth-dependence introduces an additional uncertainty on the depth-averaged velocity. Since likely values are between 80% and 100% of the surface velocity (Paterson, 1994, p. 252) we applied 90% $\pm$ 10%.

4   Interpretation and Discussion

4.1   Firn structure

In Sec. 1.2 we explained that the magnitude δ derived from Eq. 4 at free floating positions represents the amount of air contained in the ice shelf (the 'air layer thickness') if, first, the ice shelf consists in a mixture of pure ice and air only, and second, there are no gross errors in the used observations. There is no indication for a violation of these assumptions. On the contrary, the values of δ and their spatial variations as shown in Fig. 9 are in remarkable agreement with external information:

For comparison we estimate δ from density information via Eq. 3. In the bare ice region, the upper 15 m contribute only 0.6 m to δ, based on the $879 \ \mathrm{kg\,m^{-3}}$ mean density cited in Sec. 2.4. For the density below 15 m we apply two different models: a density profile of the Ross Ice Shelf (Gow, 1963) starting from $879 \ \mathrm{kg\,m^{-3}}$, and an exponential densification analogous to Eq. 14: $\rho(z) = \rho_i - (\rho_i - \rho_0)\exp(-C(z - z_0))$, with $z_0 = 15$ m,

$\rho_0 = 879$ kg m^{-3}, and $C = 0.029$ as obtained in Sec. 1.2. The resulting total air layer thicknesses are 3.6 and 2.0 m, respectively, and compare well with our model.

The increase of δ to the north corresponds to the reported northwards growing firn layer (Sec. 1.1). Moreover, the isolines of δ appear parallel to the blue ice area boundary as seen in satellite imagery (e.g., Figs. 1 and 2). Our δ values north of the increasing zone are in the 10 to 20 metres range that is reported by other authors (cf. Sec. 1.2) and they compare with the 18.7 m value derived from grounded ice core data from the region (Sec. 2.4).

We conclude that δ can be interpreted as air layer thickness to reflect the variations of firn conditions over Nivlisen.

4.2   Mass balance and basal processes

Although the spatial distribution of the mass balance calculated in Sec. 3.3 (Fig. 13a) is uncertain so that its interpretation would be speculative, we have found that in an average over a 2400 km^2 subregion of Nivlisen (34% of its total area) the net effect of basal mass balance and temporal ice mass change is -654 ± 170 kg m^{-2}a^{-1} or, equivalently, millimetres water equivalent per year. Under the steady state assumption $\partial Z_i/\partial t = 0$ this would mean basal melting of 654 kg m^{-2}a^{-1}, on an average. Basal melt rates at other Antarctic ice shelves reach several metres per year (Rignot, 2002) so that our value is within the expected range. An additional temporal change would change the basal melt rate. For example, a thinning by 100 kg m^{-2}a^{-1} would enhance the melt rate by another 100 kg m^{-2}a^{-1} while a thickening would accordingly reduce it.

A dominance of bottom melting appears very likely from our results. Melting is also reported from the two Soviet ice cores on Nivlisen (see Fig. 2): A texture analysis of the basal ice at drilling site 2 showed that no bottom freezing took place and that the ice was of meteoric origin (Korotkevich and others, 1978). For site 3, too, texture and isotope analyses indicated lasting thawing processes (Gordienko and Savatyugin,1980; Borman and Fritzsche, 1995, ch. 6) . On the other hand, basal processes may considerably vary over small scales: It has been estimated (Borman and Fritzsche, 1995, ch. 4) that an annual $13.4 \cdot 10^6$ m^3 summer meltwater runs off into the lakes in Schirmacheroasen which are linked to the ocean water beneath the ice shelf. A similar meltwater entry may occur at the tidal fractures along the grounding zone. This freshwater, being lighter than sea water, is likely to refreeze soon on the ice shelf bottom. Bottom melting in other zones may then overcompensate this local freezing and lead to the negative net effect.

Independent observations also give some indication for a possible ice thinning with time. The bare ice area on its grounded part next to the ice shelf showed a negative mass imbalance of -100 to -200 kg m^{-2}a^{-1} in the years 1991 to 1998 (Korth and others, 2000). In Schirmacheroasen, the decrease of snow patches in a decadal scale has been observed (Bormann and Fritzsche, 1995 ch. 6). An extrapolation of these signals to the ice shelf with its peculiar regimes of ice dynamics, meteorology and ice-ocean interaction is, of course, not justified. On the other hand, ice shelves may respond even more rapidly to mass imbalances than grounded ice (van der Veen, 1986). If temporal changes of the ice shelf thickness occurred, then their implications on the overall evolution of the ice shelf would be an interesting question. For example, Shepherd and others (2003) observed a progressive thinning of Larsen Ice Shelf prior to the collapse of part of it. A comparison of the present ice thickness data to historical observations is tempting but very questionable as we will explicate in the next section.

In conclusion, no quantification can be given from the present data on how bottom melting and temporal ice mass changes contribute to their negative net effect. A dominance of bottom freezing, however, seems unlikely at least for central and eastern Nivlisen.

4.3 Discrepancies to historical ice thickness observations

In 1975/1976 groups of Soviet Antarctic Expeditions performed three ice core drillings (see Fig. 2) to the bottom of the ice (Korotkevich and others, 1978). The ice thickness reported at Core 1 (374 m) agrees well with our nearby radar measurements but the reported thicknesses at Core 2 (357 m) and Core 3 (447 m) are 65 and 61 m larger, respectively, than our ice thickness model. This discrepancy is striking: At the one hand, drilling ought to be a direct and accurate thickness observation, but at the other hand, the differences far exceed the uncertainties estimated for our data.

Geophysical variations alone are an unlikely explanation: Temporal variations of more than 60 m in 20 years would be very large and are not supported by a comparison of our data to radar observations contemporary to the ice drilling (Kozlovskii and Fedorov, 1983). Spatial variations at smaller scales than our model resolution (as assessed from variations along our radar tracks) do rarely exceed 20 m in the vicinity of Core 3 and are much smaller near Core 2.

While we have tried to thoroughly assess the uncertainties of our data it is difficult to assess the reliability of the historical ice drilling observations. Tilted boreholes might

have lead to core lengths exceeding the ice thickness. E.g., a 65 m excess length at Core 2 could result from a 35° tilt which is, of course, rather large. Some discrepancies within the reports on the 1975/1976 ice drilling and radar activities remain uncommented there: Drilling site positions reported by Korotkevich and others (1978) and by Eskin and Boyarskii (1985) differ by about 6 and 4 km for Cores 1 and 3, respectively. For the position of Core 2 these two publications agree. But Kozlovskii and Fedorov (1983), in their ice thickness map derived from radar observations, mark Core 2 about 14 km away. Otherwise they would have revealed a difference in the order of -100 m between their mapped thickness and the drilled thickness.

Accepting, nonetheless, the reported ice thicknesses at the reported drilling sites 2 and 3 would lead us to two questions which we can not plausibly resolve: How are those large ice thicknesses compatible with our observed freeboard heights in view of the hydrostatic balance? And what is the horizon observed by various radar observations? A hypothesis on a marine ice bottom layer does not resolve these two questions: First, the meteoric origin of the bottom ice was reported from ice core analyses (see Sec. 4.2). Second, with a marine ice layer of, say, 65 m (corresponding to the difference between ice core and radar observations) the resulting higher total ice thickness would be incompatible to the observed freeboard height because the marine ice decreases δ only slightly (cf. Eq. 8) and, accordingly, only slightly changes the hydrostatic thickness-to-height relation (Eq. 5). Denser material transported by the ice (e.g., sediments) could resolve the problem of the hydrostatic balance but could not explain the internal horizon seen by radar observations.

We conclude that if no gross error is responsible for the described discrepancy it is most likely a peculiar coincidence of several effects such as borehole tilts, position errors, errors in our ice thickness model, small scale variations not included in this model, and temporal changes. In any case we are reserved in including the reported borehole thicknesses in a geophysical interpretation.

4.4   Snow accumulation and compaction

The evolution of the air layer thickness δ along the ice flow can be used to constrain snow accumulation and firn compaction parameters. Air contained in the ice shelf is added in accumulating snow. For example, with the accumulation rate $b_s = 300 \ \mathrm{kg\,m^{-2}a^{-1}}$ (Sec. 2.4) and a typical fresh snow density $\rho_s = 300 \ \mathrm{kg\,m^{-3}}$, the air layer thickness added by snow accumulation can be derived from Eq. 3 to be $b_s(\rho_s^{-1} - \rho_i^{-1}) = 0.67$

m a^{-1}. On the other hand, contained air escapes from the ice shelf when snow and firn are compacted, either by the continuous transformation of snow to ice or by melting with subsequent refreezing. Much of the compaction occurs shortly after accumulation. For example, Korth and Dietrich (1996) use a 600 kg m^{-3} mean density of the last year's accumulation layer. With b_s and ρ_s as above this implies that at the end of a year the accumulated snow has already been compacted by 0.5 m and retains no more than 0.17 m of air.

In analogy to the ice mass flux and balance methodology (Sec. 1.3), the net effect of contained air gain and loss is described by the divergence of the horizontal flux of contained air, div($\delta \boldsymbol{u}$). We computed the integral effect of this divergence for three areas by balancing the in- and outflow of contained air through their boundaries. We chose the areas I, II and III marked in Fig. 13 since they represent different glaciological regimes (cf. Sec. 4.1). The obtained average divergence of contained air was 0.01, 0.04, and 0.02 m a^{-1}, respectively. That is, the effect of accumulation slightly dominates over the effect of compaction and this dominance is largest in the central area II. The compaction effect in, e.g., area II is in the order of $0.04 - 0.67 = -0.63$ m a^{-1}, or, excluding the first year compaction, $0.04 - 0.17 = -0.13$ m a^{-1}.

We speculate that the obtained qualitative pattern, irrespective of its uncertainties, reveals a geophysical signal induced by spatial variations of accumulation and compaction: A higher accumulation rate in area II could result from drift snow transported by katabatic winds from further south across the ablation area. A more rapid compaction in areas I and III could result from enhanced melting and refreezing in the vicinity of the ablation area (area I) and the coast (area III). In addition, area III has a thicker firn body with a larger air content so that there is more firn to be compacted.

4.5   Ice dynamical features

The maps of ice thickness, flow velocity and, ice mass flux (Figs. 10, 7, and 12) show very clearly how the ice flow across Nivlisen is channelled between areas of local grounding or, conversely, how these grounding areas form obstacles to the ice flow leading to lower ice thicknesses in their lee. This underlines the complexity of the ice dynamical regime of Nivlisen which may be sensitive to changing grounding conditions induced by changes of either ice thickness or sea level.

5   Conclusions

Among the ice shelves along Antarctica's Atlantic coast Nivlisen is one with a peculiar glaciological regime, a long history of exploration, and a wealth of observations. The compilation and combined analysis of these data yielded a consistent geometrical and glaciological description of Nivlisen that exceeds the previous knowledge in its comprehensiveness, accuracy and detail. Among other things, we constrained the spatially varying firn conditions by utilising the hydrostatic balance relation of floating ice, and we estimated from mass flux considerations that, under a steady state assumption, basal melting with an average rate of $654 \pm 170\ \mathrm{mm\,a^{-1}}$ water equivalent occurs in a large part of the ice shelf.

Our results may be valuable for ice-dynamical modelling efforts like those of Paschke and Lange (2003) either for validating models or for providing new and improved constraints.

Our study may also serve as a starting point for investigating temporal variations: Whether and how the negative local mass balance observed upstream on the grounded ice continues on the ice shelf remains an open question relevant for understanding the dynamics of the whole Nivlisen drainage system. Additional observations and analyses could address this question: Apart from the possibility of repeated ice thickness measurements subject to the logistic constraints of Antarctic fieldwork, a further exploitation of satellite altimetry should be certainly considered. Repeated observations will be soon available from a whole sequence of altimeter missions—ERS-1, ERS-2, ENVISAT, Ice-Sat and, from 2005, CryoSat—spanning about 15 years. Advanced methods of radar altimeter analysis may use the full along-track resolution and include several altimetric waveform parameters, thus facilitating the separation of real surface height changes from changes in firn conditions (Legrésy and others, 2000). Repeated GPS measurements could serve as ground truth. In such analyses of originally ellipsoidal height data the exact knowledge of vertical displacements due to ocean tides and the inverse barometric effect is of great value. New information on bottom processes could be gained from more sophisticated radar applications (Corr and others, 2002). An extension of mass flux and mass balance observations at western Nivlisen including a mass flux estimation across the southwestern grounding line, is another open issue.

In view of the extensive knowledge already available and also of the favourable logistic conditions it seems worthwhile to pursue the open questions on Nivlisen and its drainage

basin as a case study on the complex interactions of land ice, bedrock, ice shelf, ocean, and atmosphere.

Acknowledgements

References

Baessler, M., R. Dietrich and C. K. Shum. 2003. Investigations of Ice Dynamics at the Grounding Zone of an Antarctic Ice Shelf Utilizing SAR-Interferometry. In *Proc. Weikko A. Heiskanen Symp. in Geodesy, 1-4 Oct 2002, Columbus, Ohio, USA.*

Bamber, J. and C. R. Bentley. 1994. A comparison of satellite-altimetry and ice-thickness measurements of the Ross Ice Shelf, Antarctica. *Ann. Glaciol.*, 20, 357–364.

Bamber, J. L. and A. J. Payne, editors. 2003. *Mass Balance of the Cryosphere.* Cambridge University Press.

Bormann, P. and D. Fritzsche, editors. 1995. *The Schirmacher Oasis, Queen Maud Land, East Antarctica, and its surroundings.* Justus Perthes Verlag, Gotha.

Boyarskii, V. I., B. A. Nikitin and V. P. Stepanov. 1983. Determination of the grounding line of the Novolazarevskaya Ice Shelf by radio echo sounding. *Trudy AANII*, 379, 54–58.

Brenner, A. C., R. A. Bindschadler, R. Thomas and H. Zwally. 1983. Slope-induced errors in radar altimetry over continental ice sheets. *J. Geoophys. Res.*, 88(C3), 1617–1623.

Brisset, L. and F. Rémy. 1996. Antarctic topography and kilometre-scale roughness derived from ERS-1 altimetry. *Ann. Glaciol.*, 23, 374–381.

Budd, W. F., M. J. Corry and T. H. Jacka. 1982. Results from the Amery Ice Shelf Project. *Ann. Glaciol.*, 3, 36–41.

Corr, H. F. J., A. Jenkins, K. W. Nicholls and C. S. M. Doake. 2002. Precise measurement of changes in ice-shelf thickness by phase-sensitive radar to determine basal melt rates. *Geophys. Res. Lett.*, 29(8), 1232–1235, doi:10.1029/2001GL014618.

Coslett, P. H., M. Guyatt and R. H. Thomas. 1975. Optical levelling across an Antarctic ice shelf. *Br. Antarct. Surv. Bull.*, 40, 55–63.

Damm, V. and D. Eisenburger. 2004. Ice thicknesses and subice morphology in central Queen Maud land deduced by radio echo soundings (RES). *Geologisches Jahrbuch, Serie E.* to appear.

Dietrich, R., R. Dach, W. Korth, J. Polzin and M. Scheinert. 1998. Gravimetric earth tide observations in Dronning Maud Land/Antarctica to verify ocean tidal loading. In Ducarme, B. and Paquet, P., editors, *Proc. 13th Int. Symp. on Earth Tides, Brussels, July 22-25, 1997*, pages 529–536, Brussels. Obs. Royal de Belgique.

Dietrich, R., G. Liebsch, H.-J. Dittfeld and G. Noack. 1995. Ocean tide and attempt of Earth tide recordings at Schirmacher Oasis / Dronning Maud Land (Antarctica). In *Proc. 12th Int. Symp. on Earth Tides, Beijing, August 4–7, 1993*, pages 563–569, Beijing. Science Press.

Eskin, L. I. and V. I. Boyarskii. 1985. Some morphometric characteristics of the Novolazarevskaya Ice Shelf. *Problemy Arktiki i Antarktiki*, 59, 56–60. (in Russian).

Fritzsche, D. 1996. Geophysikalische Untersuchungen in der Umgebung der Schirmacheroase, Februar bis April 1995. In Wand, U., editor, *Studies of the AWI Research Department Potsdam in Antarctica, 1994/95*, volume 215 of *Reports on Polar Res.*, pages 127–136. Alfred-Wegener-Institut für Polar- und Meeresforschung, Bremerhaven.

Fritzsche, D. 2005. Gravimetric Profiling in Central Dronning Maud Land, East Antarctica. *Geologisches Jahrbuch, Serie E*. to appear.

Goldstein, R. M., H. A. Zebker and C. L. Werner. 1988. Satellite radar interferometry: Two-dimensional phase unwrapping. *Radio Science*, 23(4), 713–720.

Gordienko, V. G. and S. M. Savatyugin. 1980. Results of the oxygen isotope analysis on an ice core from the Novolazarevskaya Ice Shelf. *Inf. Byull. Sov. Antarkt. Eksped.*, 100, 85–90. (in Russian).

Gow, A. J. 1963. The inner structure of the Ross Ice Shelf at Little America V, Antarctica, as revealed by deep core drilling. *Int. Assoc. Sci. Hydrol.*, 61, 272–284.

Hanssen, R. F. 2001. *Radar Interferometry: Data Interpretation and Error Analysis*. Kluwer, Dordrecht.

Jenkins, A. and C. S. M. Doake. 1991. Ice-ocean interaction on Ronne Ice Shelf, Antarctica. *J. Geophys. Res.*, 96(C1), 791–813.

Jezek, K. and RAMP Product Team. 2002. RAMP AMM-1 SAR Image Mosaic of Antarctica. Fairbanks, AK: ASF, in association with the NSIDC, Boulder, CO. Digital media.

Khokhlov, G. P. 1984. Distribution of Electrical Parameters in Upper Layers of Shelf, Land, and Fast Ice Near Novolazarevskaya Station. *IEEE J. Ocean. Engin.*, 9(5), 360–365.

Kislov, B. V., L. N. Manevskii and L. M. Savatyugin, 1983. Glaciological research in the area of Novolazarevskaya Station. *Trudy Sov. Antarkt. Eksped.*, 76, 125–130. (in Russian).

Korotkevich, E. S., L. M. Savatyugin and V. A. Morev, 1978. Drilling through the ice shelf in the vicinity of Novolazarevskaya Station. *Inf. Byull. Sov. Antarkt. Eksped.*, 98, 49–52. (in Russian).

Korth, W. and R. Dietrich. 1996. *Ergebnisse geodätischer Arbeiten im Gebiet der Schirmacheroase/Antarktika 1988 – 1993*. Number 301 in DGK Reihe B. Deutsche Geodätische Kommission, München.

Korth, W., R. Dietrich, G. Reitmayr and V. Damm. 1998. Regional geoid improvement based on surface gravity data. In *Geodesy on the Move, Gravity, Geoid, Geodynamics, and Antarctica. IAG Scientific Assembly, Rio de Janeiro, 1997*, volume 119 of *IAG Symposia*, Heidelberg. Springer-Verlag.

Korth, W., J. Perlt and R. Dietrich. 2000. Ergebnisse geodätisch-glaziologischer Feldarbeiten während der Expedition 1998 in der Region der Schirmacheroase. In Dietrich, R., editor, *Deutsche Beiträge zu GPS-Kampagnen des Scientific Committee on Antarctic Research (SCAR) 1995–1998*, number 310 in DGK Reihe B, pages 219–227. Deutsche Geodätische Kommission, München.

Kozlovskii, A. M. and B. A. Fedorov. 1983. Characterizing glaciation and subglacial relief of the Princess Astrid Coast by results of radio-echo sounding. *Trudy AANII*, 379, 58–62. (in Russian).

Legrésy, B., F. Rémy and P. Vincent. 2000. Is the South Greenland Dome Moving Westward? *Geophys. Res. Abstracts*, 2.

Lemoine, F. G. and others. 1996. The Development of the NASA GSFC and NIMA Joint Geopotential Model. In *Proc. of the Int. Symp. on Gravity, Geoid and Marine Geodesy, Tokyo, 1996*, Berlin. Springer.

Metzig, R., R. Dietrich, W. Korth, J. Perlt, R. Hartmann and W. Winzer. 2000. Horizontal Ice Velocity Estimation and Grounding Zone Detection in the Surrounding of Schirmacheroase, Antarctica, Using SAR Interferometry. *Polarforschung*, 67(1/2), 7–14.

Meyer, U., D. Steinhage, U. Nixdorf and H. Miller. 2004. Airborne radio echo sounding measurements from Novolazarevskaya Skiway, central Dronning Maud Land, Antarctica. *Geologisches Jahrbuch, Serie E.* to appear.

Paschke, B. and M. A. Lange. 2003. Dynamics and mass balance of the ice sheet/ice shelf regime at Nivlisen, Antarctica, as derived from a coupled three-dimensional numerical flow model. *Ann. Glaciol.*, 37, 159–165.

Paterson, W. S. B. 1994. *The Physics of Glaciers*. Butterworth-Heinemann, Oxford, third edition.

Rabus, B. T. and O. Lang. 2002. On the representation of ice-shelf grounding zones in SAR interferograms. *J. Glaciol.*, 48(162), 345–356.

Reigber, C. and others. 2005. Earth Gravity Field and Seasonal Variability from CHAMP. In Reigber, C., Lühr, H., Schwintzer, P., and Wickert, J., editors, *Earth Observation with CHAMP: Results from Three Years in Orbit*, pages 25–30. Springer, Berlin.

Reitmayr, G. 1996. Bericht über gravimetrische Messungen und sie begleitende GPS-Ortsbestimmungen im Königin Maud Land, Antarktis, während der Expedition GeoMaud. Archiv Nr.: 114900. Technical report, Bundesanstalt für Geowissenschaften und Rohstoffe, Hannover.

Rémy, F., P. Shaeffer and B. Legrésy. 1999. Ice Flow Physical Processes derived from ERS-1 high-resolution map of Antarctica and Greenland ice sheet. *Geophys. J. Int.*, 139, 645–656.

Renner, R. G. B. 1969. Surface elevations on the Larsen Ice Shelf. *Br. Antarct, Surv. Bull.*, 19, 1–8.

Rignot, E. 2002. East Antarctic Glaciers and Ice Shelves Mass Balance from Satellite Data. *Ann. Glaciol.*, 34, 217–227.

Scharroo, R., P. N. A. M. Visser and G. J. Mets. 1998. Precise orbit determination and gravity field improvement for the ERS satellites. *J. Geophys. Res.*, 103(C4), 8113–8127.

Shabtaie, S. and C. R. Bentley. 1982. Tabular icebergs: implications from geophysical studies of ice shelves. *J. Glaciol.*, 28(100), 413–430.

Shabtaie, S. and C. R. Bentley. 1987. West Antarctic ice streams draining into the Ross Ice Shelf: configuration and mass balance. *J. Geophys. Res.*, 92(B2), 1311–1336.

Shepherd, A., D. Wingham, T. Payne and P. Skvarca. 2003. Larsen Ice Shelf Has Progressively Thinned. *Science*, 302, 856–859.

Simonov, I. M. 1971. *The oases of East Antarctica*. Gidrometeoizdat, Leningrad. (in Russian).

Smith, D. A. 1998. There is no such thing as "The" EGM96 geoid: Subtle points on the use of a global geopotential model. *International Geoid Service Bulletin*, 8, 17–28.

Steinhage, D., U. Nixdorf, U. Meyer and H. Miller. 1999. New maps of the ice thickness and subglacial topography in Dronning Maud Land, Antarctica, determined by means of airborne radio-echo sounding. *Ann. Glaciol.*, 29, 267–272.

Tapley, B. D., S. Bettadpur, M. Watkins and C. Reigber. 2004. The gravity recovery and climate experiment: Mission overview and early results. *Geophys. Res. Lett.*, 31(9). doi:10.1029/2004GL019920.

Thyssen, F. 1988. Special aspects of the central part of Filchner-Ronne Ice Shelf. *Ann. Glaciol.*, 11, 173–179.

Thyssen, F. and K. Grosfeld. 1988. Ekström Ice Shelf, Antarctica. *Ann. Glaciol.*, 11, 180–183.

van der Veen, C. J. 1986. Numerical modelling of ice shelves and ice tongues. *Annales Geophysicae*, 4B(1), 45–54.

Vaughan, D. G., J. Sievers, C. S. M. Doake, H. Hinze, D. T. Mantripp, V. S. Pozdeev, H. Sandhäger, H. W. Schenke, A. Solheim and F. Thyssen. 1995. Subglacial and seabed topography, ice thickness and water column thickness in the vicinity of Filchner-Ronne-Schelfeis, Antarctica. *Polarforschung*, 64(2), 75–88.

Wessel, P. and W. Smith. 1991. Free software helps map and display data. *EOS Trans. AGU*, 72, 441.

Wiehl, M. and R. Dietrich. 2000. Statistical analysis of snow and ice surface structures and some conclusions on microwave signal scattering. *Geophys. Res. Abstracts*, 2.

Table 1: Error budget (one-sigma errors in metre) of the ellipsoidal height and freeboard height models of Sec. 2.2.3 (representing 3.7 km scale averages). Numbers in brackets refer to positions near the model domain boundary and the ice rumple about 10.7°E, −70.4°S.

	spatial variations	absolute level	total
altimetric data	0.4		
temporal SST variations	0.2		
limited resolution and coverage of measurements	0.5 (1.5)		
ellipsoidal height model	0.67 (1.6)		
geoid	0.07	0.5	0.505
mean SST	0.14	0.3	0.33
freeboard height model	0.69 (1.6)	0.58	0.90 (1.7)

Table 2: Analysed SAR scenes for the interferograms I_1 and I_2 (cf. Fig. 1) consisting of 3 frames each.

Date	Sat.	Orbit	Track	Base	Pass	Interfer.
5/08/1996	ERS-1	25168				
5/09/1996	ERS-2	5495	130	51 m	asc.	I_1
5/20/1996	ERS-1	25354				
5/21/1996	ERS-2	5681	316	6 m	asc.	I_2

Table 3: Error budget (one-sigma errors, propagated from the input errors) for the model of the 'apparent air layer thickness' δ (cf. Sec. 3.1). Pairs of numbers separated by '/' represent different values for north and south of $-70.35°$ latitude.

input, or error source	error of input spatial variations	absolute level	reference	resulting error for the δ model (m) spatial variations	absolute level	total
Z	4.9 m / 21 m		Sec. 2.1	0.6 / 2.5		0.6 / 2.5
h	0.69 m	0.58 m	Sec. 2.2.3	0.77	0.65	1.0
ρ_w		1.5 $\mathrm{kg\,m^{-3}}$	Sec. 2.4	0.15	0.48	0.5
ρ_i		3 $\mathrm{kg\,m^{-3}}$	Sec. 2.4	0.34	1.1	1.3
inter- and extrapolation			Sec. 3.1	2.0 / 1.0		2.0 / 1.0
total error				2.3 / 2.8	1.4	2.7 / 3.2

Table 4: Ice mass balance components and their uncertainties for the areas A, B and C marked in Fig. 12. See Sec. 3.3 for further explanations.

		A	B	C	total	
in-flux	($10^9\mathrm{kg\,a^{-1}}$)	844 ± 150	709 ± 130	1229 ± 160	$2073 \pm$	220
out-flux	($10^9\mathrm{kg\,a^{-1}}$)	647 ± 130	331 ± 50	709 ± 130	$978 \pm$	140
lateral in- and out-flux	($10^9\mathrm{kg\,a^{-1}}$)	0 ± 200	0 ± 90	0 ± 170	$0 \pm$	220
$\iint (b_s + b_b - \rho_i\partial Z_i/\partial t)\, d\sigma$	($10^9\mathrm{kg\,a^{-1}}$)	-197 ± 280	-378 ± 170	-520 ± 270	$-1095 \pm$	340
area (grounded part in brackets)	($\mathrm{km^2}$)	1102	735	724 (122)	2561 (122)	
mean of $b_s + b_b - \rho_i\partial Z_i/\partial t$	($\mathrm{kg\,m^{-2}a^{-1}}$)	-179 ± 260	-515 ± 230	-719 ± 370	$-427 \pm$	130
mean of b_s (from Sec. 2.4)	($\mathrm{kg\,m^{-2}a^{-1}}$)	300 ± 100	300 ± 100	$-67^{[a]} \pm 100$	$196 \pm$	100
mean of $b_b - \rho_i\partial Z_i/\partial t$	($\mathrm{kg\,m^{-2}a^{-1}}$)	-479 ± 280	-815 ± 250	$-783^{[b]} \pm 460$	$-654^{[b]} \pm$	170

[a] resulting from accumulation ($+300$) in the northern third and ablation (-250) in the southern two thirds of area C

[b] here the integral mass balance is divided by the floating area only. E.g. for area C, $\frac{-520\cdot10^9\mathrm{kg\,a^{-1}} - (-67\mathrm{kg\,m^{-2}a^{-1}}\cdot724\mathrm{km^2})}{(724-122)\mathrm{km^2}}$
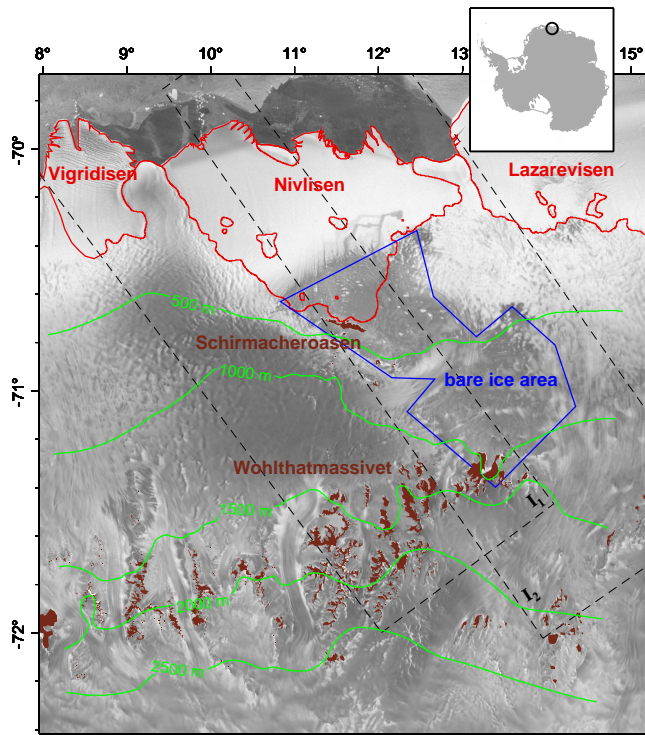
Figure 1: The region of Schirmacheroasen with Nivlisen. Grounding lines and the ice front *(red lines)*, ice surface heights *(green)*, the bare ice area *(blue)* and open rocks *(brown)* are indicated. The background image is the RADARSAT amplitude image (Jezek and RAMP Product Team, 2002). Dashed lines indicate two ERS-1/2 SAR interferograms used in Sec. 2.3.
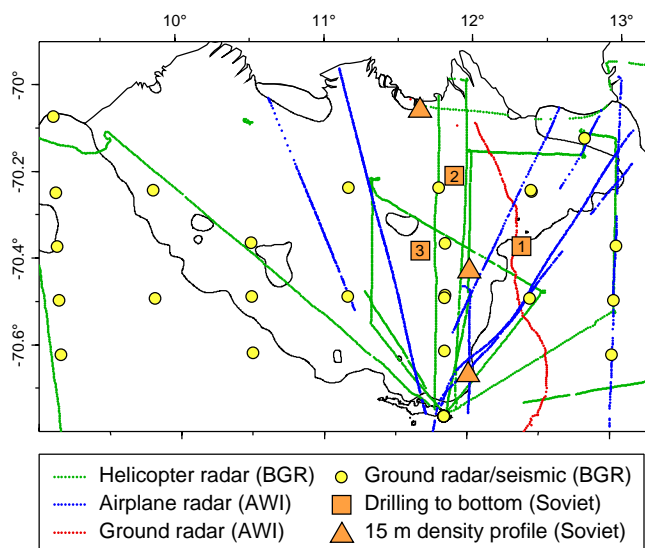

Figure 2: Ice thickness and firn observations. The drilling site positions are after Korotkevich and others (1978). The positions of 15 m density profiles are estimates after the verbal description by Khokhlov (1984).
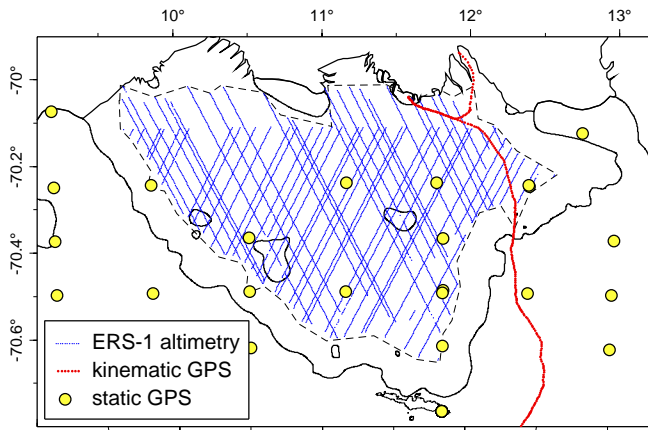
Figure 3: Ellipsoidal height observations. The thin dashed line indicates the domain of the model derived from these observations (Sec. 2.2.3).
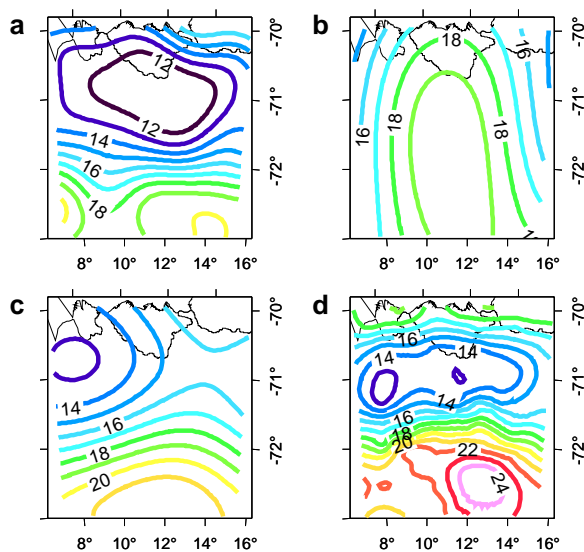
Figure 4: The geoid (in metres) in the region of Schirmacheroasen according to *(a)* EGM96 (Lemoine and others, 1996), *(b)* the CHAMP model EIGEN-3p (Reigber and others, 2005), *(c)* the GRACE model EIGEN-GRACE01S (Tapley and others, 2004), and *(d)* the regional geoid model (Korth and others, 1998).
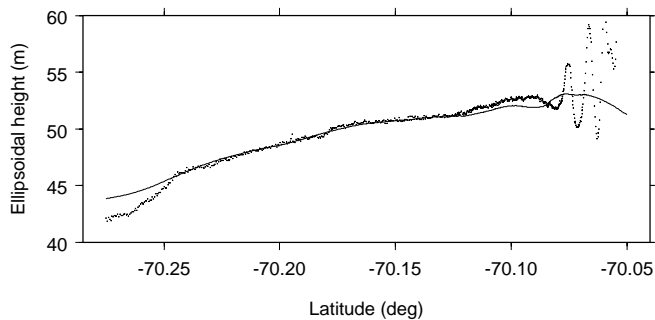
Figure 5: Comparison of heights from kinematic GPS measurements *(dots)* and from the altimetric model *(line)* along the traverse.

31
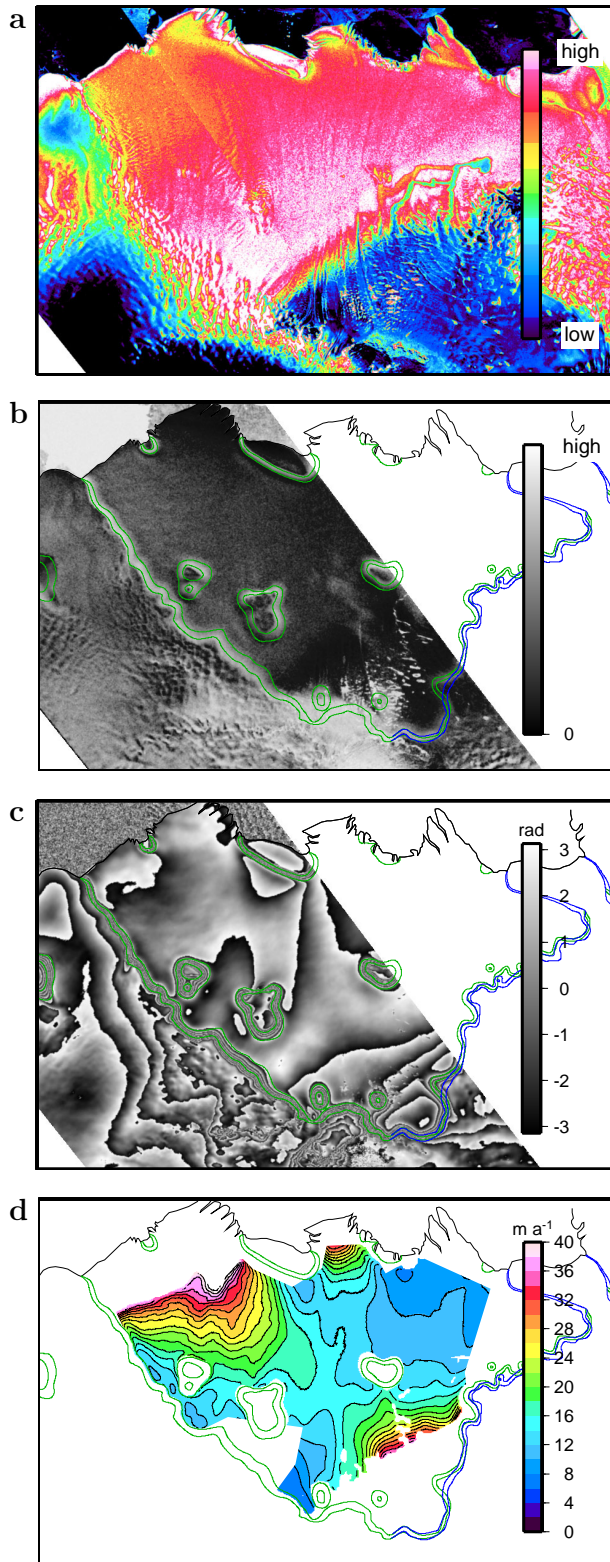
Figure 6: Steps of the SAR processing. *(a)* Amplitude image. The flowline structures were used to infer flow direction. *(b)* Phase gradients of interferogram I_1. They indicate that internal deformations of the ice shelf are low, except for grounding zones. Coloured lines show approximate borders of deformation zones. At some places they are different for low tide (green) and high tide (blue). *(c)* The corrected interferogram I_1 showing clear fringe belts at the grounding zones. Drawn-out fringes over the shelf area reflect the horizontal velocity. *(d)* An error estimate of the derived horizontal flow velocity is obtained by error propagation.
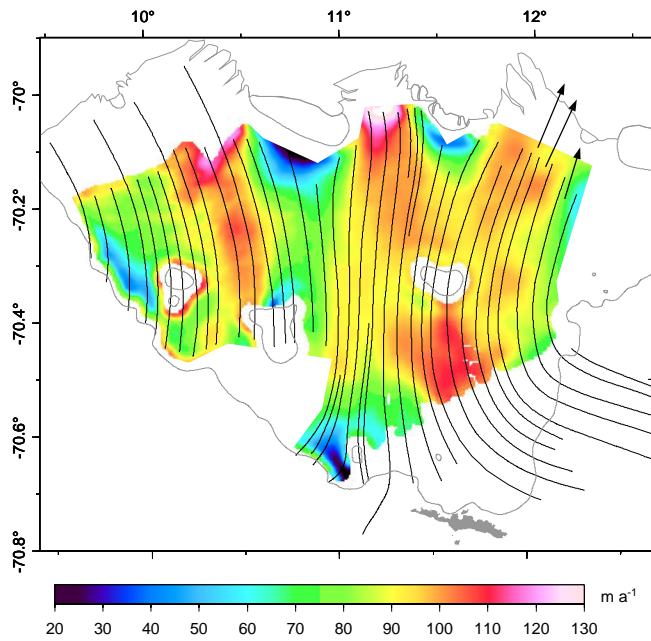
Figure 7: Horizontal velocity field of Nivlisen derived from interferometric SAR processing. Black lines are flowlines deduced from the amplitude image and used to define the flow direction. Arrows show the GPS measurements used for the calibration.
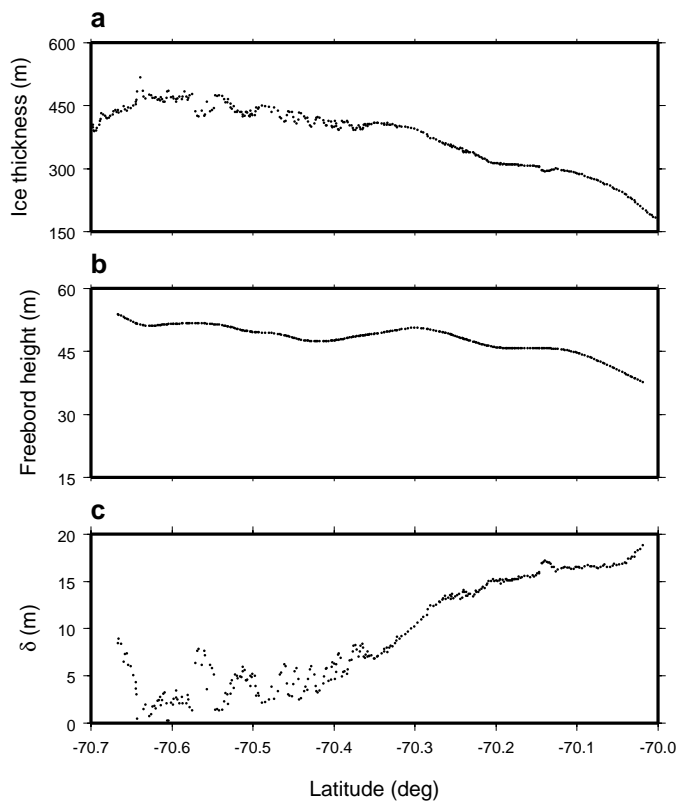
Figure 8: *(a)* Measured ice thicknesses, *(b)* freeboard heights interpolated from the model of Sec. 2.2.3, and *(c)* derived values of the 'apparent air layer thickness' δ along the AWI airplane radar track going to the ice tongue at 11.2°E (cf. Fig. 2)

33
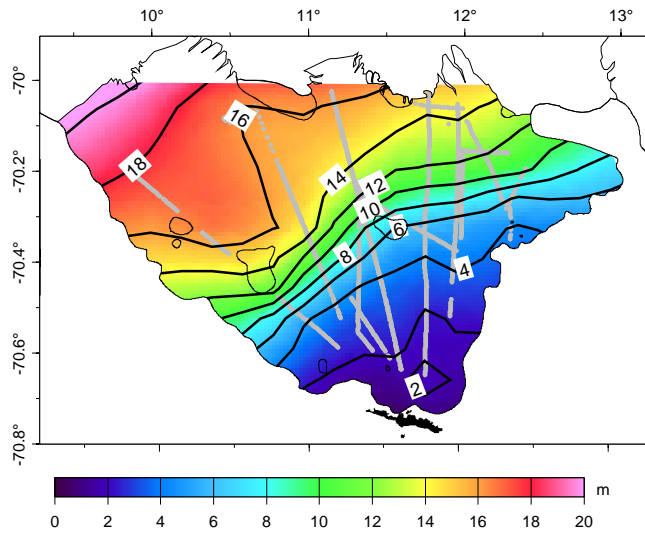
Figure 9: Model of the 'apparent air layer thickness' δ (in metres) derived from ice thickness and freeboard height data at the positions indicated in gray.
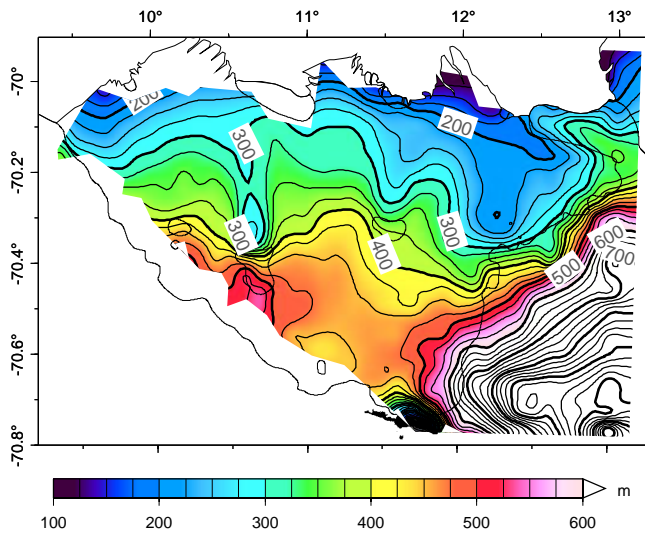

Figure 10: Ice thickness model (in metres) derived from direct ice thickness observations and from height observations converted to ice thickness through the hydrostatic balance relation. Contour intervals are 25 m.
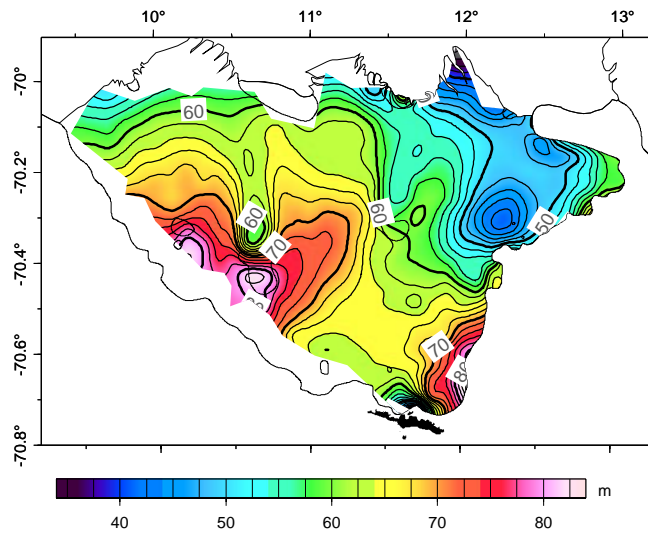
Figure 11: Ellipsoidal height model (in metres) derived from both direct height observations and ice thickness observations converted to heights. Contour intervals are 2.5 m.
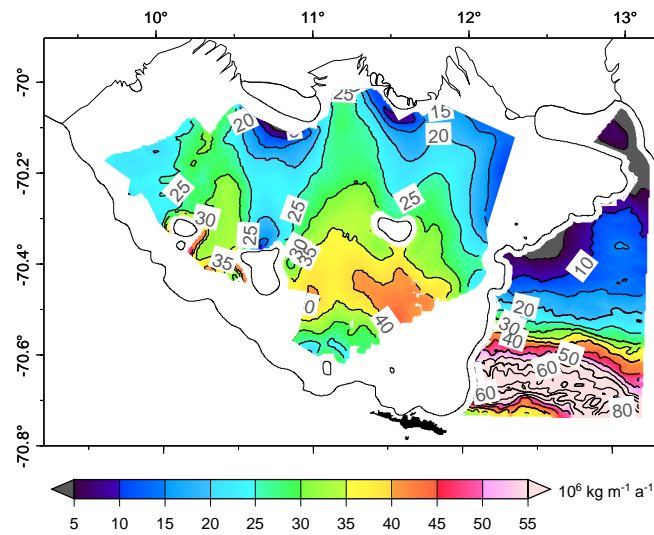

Figure 12: Horizontal ice mass flux (absolute value in 10^6 $\mathrm{kg\,m^{-1}a^{-1}}$) computed from the ice thickness model and the ice flow velocity field.
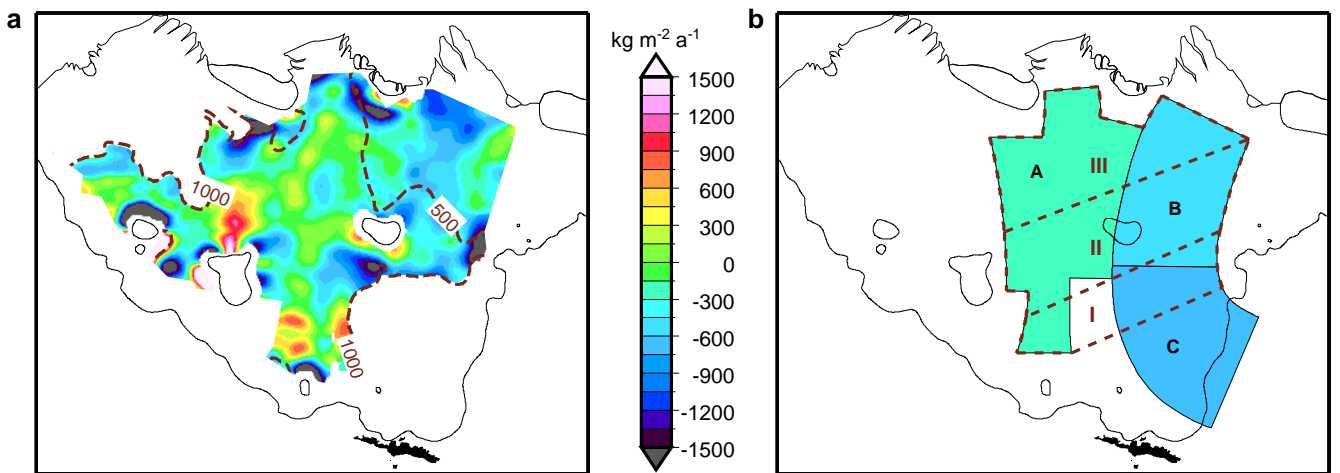
Figure 13: Net effect of specific mass balance and local mass balance, $b_s + b_b - \rho_i \partial / \partial t Z_i$ (in $\mathrm{kg\,m^{-2}a^{-1}}$). *(a)* Map computed from the local ice mass flux divergence. Dashed brown contours show the spatially varying accuracy. *(b)* The areas A, B, C of the integrated mass balance evaluation with areally mean values colour-coded. The areas I, II, III (dashed brown lines) are referred to in Sec. 4.4.